JGR Solid Earth

RESEARCH ARTICLE
10.1029/2020JB021128

Imaging the Subsurface Plumbing Complex of Steamboat Geyser and Cistern Spring With Hydrothermal Tremor Migration Using Seismic Interferometry

Sin-Mei Wu[1], Fan-Chi Lin[1,2], Jamie Farrell[1], William E. Keller[3], Erin B. White[3], and Jefferson D. G. Hungerford[3]

[1]Department of Geology and Geophysics, University of Utah, Salt Lake City, UT, USA, [2]Institute of Earth Sciences, Academia Sinica, Taipei, Taiwan, [3]National Park Service, Yellowstone Center for Resources, Yellowstone National Park, WY, USA

Key Points:

- We develop an interferometric-based polarization analysis to investigate high-resolution spatiotemporal pattern of hydrothermal tremor
- We construct the first image of the plumbing architecture for the Steamboat–Cistern system to a depth of 140 m
- We illuminate the recharge evolution of Steamboat Geyser and Cistern Spring and the dynamic subsurface interaction between the two features

Correspondence to:
S.-M. Wu,
sinmei.wu@utah.edu

Citation:
Wu, S.-M., Lin, F.-C., Farrell, J., Keller, W. E., White, E. B., & Hungerford, J. D. G. (2021). Imaging the subsurface plumbing complex of Steamboat Geyser and Cistern Spring with hydrothermal tremor migration using seismic interferometry. *Journal of Geophysical Research: Solid Earth*, *126*, e2020JB021128. https://doi.org/10.1029/2020JB021128

Received 13 OCT 2020
Accepted 22 FEB 2021

Abstract Steamboat Geyser in Yellowstone National Park is the tallest active geyser on Earth and is believed to have hydrologic connection to Cistern Spring, a hydrothermal pool ~100 m southwest from the geyser vent. Despite broad scientific interest, rare episodic Steamboat eruptions have made it difficult to study its eruption dynamics and underground plumbing architecture. In response to the recent reactivation of Steamboat, which has produced more than 130 eruptions since March 2018, we deployed a dense seismic nodal array surrounding the enigmatic geyser in the summer of 2019. The array recorded abundant 1–5 Hz hydrothermal tremor originating from phase-transition events within both Steamboat Geyser and Cistern Spring. To constrain the spatiotemporal distribution of the tremor sources, an interferometric-based polarization analysis was developed. The observed tremor locations indicate that the conduit beneath Steamboat is vertical and extends down to ~120 m depth and the plumbing of Cistern includes a shallow vertical conduit connecting with a deep, large, and laterally offset reservoir ~60 m southeast of the surface pool. No direct connection between Steamboat and Cistern plumbing structures is found. The temporal variation of tremor combined with *in situ* temperature and water depth measurements of Cistern reveals interaction between Steamboat and Cistern throughout the eruption/recharge cycles. The observed delayed responses of Cistern Spring in reaction to Steamboat eruptions and recharge suggest that the two plumbing structures may be connected through a fractured/porous medium instead of a direct open channel, consistent with our inferred plumbing structure.

1. Introduction

Steamboat Geyser in Yellowstone National Park is the tallest active geyser on Earth—recorded eruption heights have exceeded 110 m since 1962 (Reed et al., 2021; White et al., 1988). In addition to the fascinating water discharge phase lasting less than an hour after the onset of an eruption, Steamboat earned its name from the roaring steam phase that could create a steam column hundreds-of-meters high above the ground and persist for days (White et al., 1988). Steamboat's major eruptions are episodic with only three major active phases recorded: in the 1960s, 1980s, and the ongoing eruptions since March 2018. The current active phase has had more than 130 eruptions to date that have been hypothesized to be associated with shallow magmatic volatile accumulation (Wicks et al., 2020) but the exact mechanism remains inconclusive (Reed et al., 2021). Sporadic eruptions did occur between active phases but most of these eruptions were not directly witnessed and only were accounted for after the fact. The recorded latest singular eruption before the current active phase was in 2015. Since 1966, Cistern Spring, located 100 m southwest of Steamboat, was observed to have its water level drop (by 5–7 m) and surface temperature decrease (about 20°) after major eruptions of Steamboat (White et al., 1975), suggesting these two features are interconnected. Such hydrologic connection persists in the current active phase; however, the exact location where Steamboat and Cistern are physically connected and how the interaction of the two might affect the eruption/recharge dynamics of Steamboat remain largely elusive.

The plumbing geometry of a geyser can be complex and exerts direct control over its eruption and recharge dynamics (Hurwitz & Manga, 2017). Narrow constrictions make the supersonic (choked) flow possible for eruptions, and the depth extent of the fluid pathway including the reservoir location governs the vapor mass fraction in the system before an eruption, which is indicative of exit velocity that controls the eruption

height (Karlstrom et al., 2013; Kieffer, 1989; Reed et al., 2021). Shallow reservoirs or cavities that allow the vapor and liquid two-phase mixture to accumulate have been proposed to modulate a geyser's eruptive characteristics (i.e., preplay, minor, and major eruptions) and may be responsible for the geyser's (ir)regularity (Adelstein et al., 2014; Belousov et al., 2013; Munoz-Saez, Manga, et al., 2015; Rudolph et al., 2018; Vandemeulebrouck et al., 2014). Side channels and offset reservoirs/cavities have been proposed or found in Old Faithful Geyser (Hutchinson et al., 1997; Vandemeulebrouck et al., 2013; Wu et al., 2017), Lone Star Geyser (Nayak et al., 2020; Vandemeulebrouck et al., 2014) in Yellowstone, Geyser Valley in Russia (Belousov et al., 2013), Strokkur Geyser in Iceland (Eibl et al., 2020), and El Jefe in Chile (Ardid et al., 2019). A permeable medium that allows pressure transmission has been inferred to govern the interaction between nearby hydrothermal features (e.g., El Tatio in Chile; Munoz-Saez, Namiki, et al., 2015). The conduits of natural geysers are irregular, contorted, and can contain structures that are 2 orders of magnitude different in scale (e.g., centimeter choke point vs. meter wide cavity; Belousov et al., 2013; Hutchinson et al., 1997), which pose significant challenges in geophysical imaging.

In situ physical probes such as temperature, pressure loggers, and video cameras have been used to depict the direct portrayal and physical condition of shallow conduits in geysers (Belousov et al., 2013; Hutchinson et al., 1997; Munoz-Saez, Manga, et al., 2015; Munoz-Saez, Namiki, et al., 2015; Walter et al., 2018; White et al., 1988). However, the depth extent of such measurements has been hampered by constrictions and lateral turns thereby limiting them to ~25 m depth at most. Ground penetrating radar is not only able to image high-resolution spatiotemporal fluid distribution but also restricted to mapping only the shallowest part of the system (e.g., <5 m for Old Faithful; Lynne et al., 2018). Resistivity studies from electromagnetic surveys are widely applied for geothermal exploration but the fine-scale study of a hydrothermal system's plumbing has been less common (e.g., Carr et al., 2019).

Early seismic studies mainly focused on understanding the source origin of the hydrothermal tremor (e.g., bubble collapse and nucleation) and their relation to a geyser's recharge and eruption dynamics (Kedar et al., 1996, 1998; Kieffer, 1984, 1989; Rinehart, 1965). During recharge, bubbles form or collapse in response to changes in temperature and hydrostatic pressure within the water column, which progressively brings heat from depth as the rise of less-dense bubbles is driven by buoyancy (Vandemeulebrouck et al., 2014; Wu et al., 2019). When the entire column is close to the saturation temperature, small pressure perturbations from the surficial preplay activity reduce the hydrostatic pressure and give rise to boiling in the deep conduit by lowering the boiling temperature, thus an eruption can occur (Kieffer, 1989).

With the recent availability of multiple instruments and array data, subsurface hydrothermal structures such as major reservoirs and the local geologic deposits can now be inferred using both active source (Ardid et al., 2019; Caylor, 2020; Price et al., 2015) and passive (Wu et al., 2017) seismic imaging methods. Spatiotemporal patterns of the source locations of hydrothermal tremor can be further used to illuminate high-resolution plumbing geometry and recharge/eruption dynamics. For example, shallow and laterally shifted reservoirs are proposed based on ground deformation (using long-period seismic data) induced from subsurface offset pressure sources at El Jefe in Chile (Ardid et al., 2019), and based on the locations of high-frequency tremor (>10 Hz) at Old Faithful and at Lone Star Geysers in Yellowstone (Vandemeulebrouck et al., 2013, 2014). Temporal changes in the resonant frequency of tremor also reveal the oscillatory fluid behavior between the conduit and offset reservoir (Rudolph & Sohn, 2017; Rudolph et al., 2018; Vandemeulebrouck et al., 2013). While high-frequency tremor energy is predominant in seismic records, weak low-frequency tremor (1–5 Hz) was initially discovered at Old Faithful Geyser where it solely provided insight into the deep plumbing system (20–80 m depth) and illustrated the full recharge evolution from the 4D view of tremor (Wu et al., 2019).

In this study, following our earlier study of Old Faithful (Wu et al., 2019), we investigate the plumbing architecture of the Steamboat–Cistern system by imaging the hydrothermal tremor source migration. In response to the recent rejuvenation of Steamboat, we deployed two dense seismic arrays; one in May–June 2018 (Farrell & Lin, 2018) and one in June–July 2019 (Farrell & Lin, 2019) to record the active eruptions. The 2019 data, which will be the focus of this study, cover six eruption cycles and have a larger array aperture compared to the 2018 array. In Section 2, we introduce the array design and identify distinct 1–5 Hz tremor excited by Steamboat and Cistern. In Section 3, we describe the interferometric-based method that we develop to simultaneously locate the tremor in both space and time. In Section 4, we summarize the

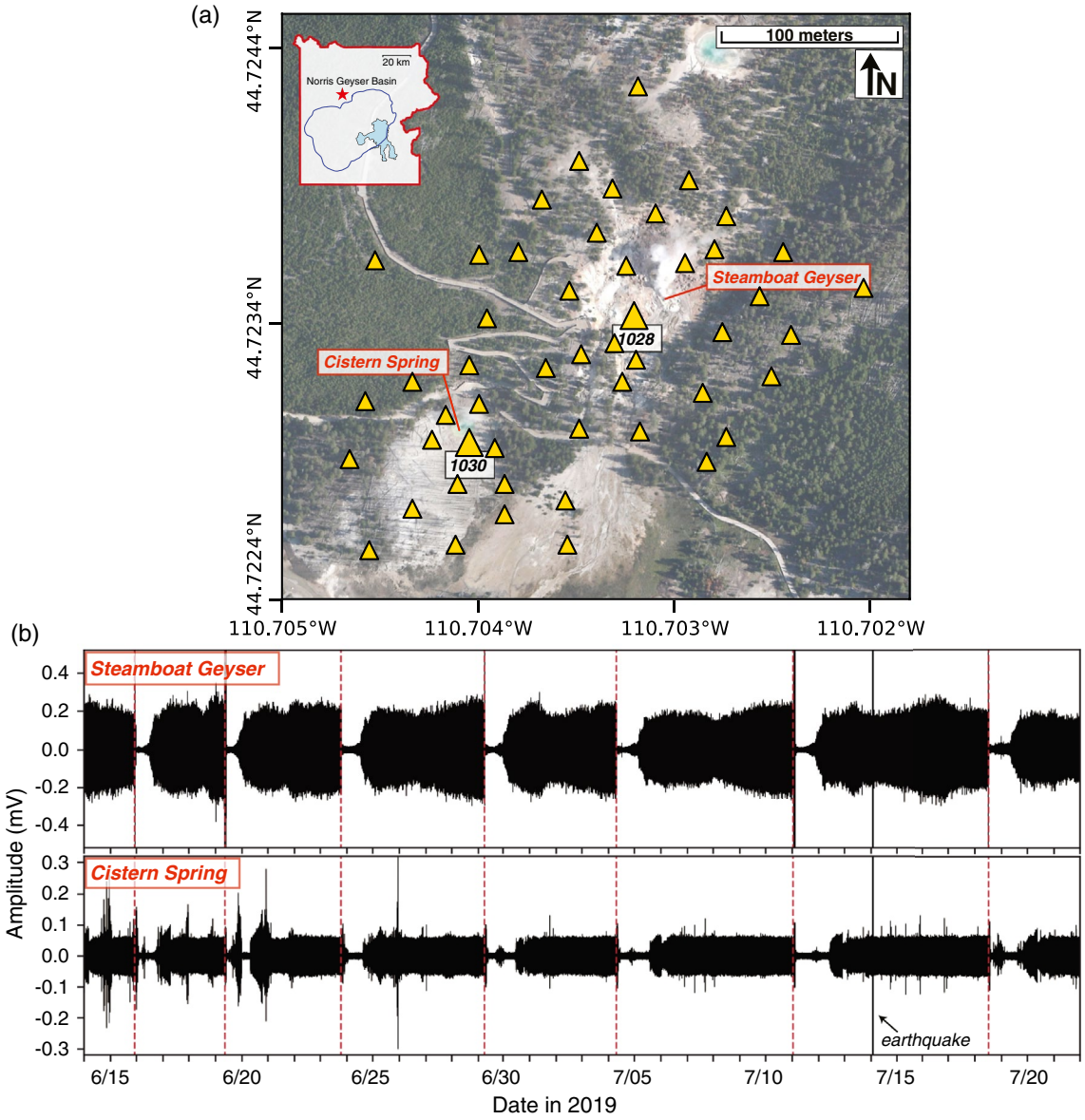

Figure 1. (a) The seismic nodal array deployed between June 13 and July 22 2019. The yellow triangles represent the station locations. The red star in the upper-left inset denotes the location of Norris Geyser Basin where Steamboat is located within Yellowstone National Park (red boundary). The blue line in the inset delineates the boundary of the 0.63-Ma caldera. (b) The month-long, 1–5 Hz seismic energy associated with steam–liquid phase transition emitted from Steamboat Geyser (station 1028) and Cistern Spring (station 1030). The red-dashed lines mark the Steamboat eruption times obtained from GeyserTimes (2020). The unit of the seismogram without removing the instrument response is millivolt.

observed 4D pattern of tremor sources and the plumbing architecture of both features. In Section 5, we discuss the implications of the recharge/eruption dynamics and the plumbing connection between the two systems based on the seismic results and *in situ* observations.

2. Data

2.1. Seismic Nodal Array and *In Situ* Transducers

In collaboration with the National Park Service (NPS) at Yellowstone, we deployed a seismic nodal array in the vicinity of Steamboat Geyser and Cistern Spring between June 13 and July 22, 2019 (Figure 1a). The array was composed of 50 three-component 5-Hz geophones with a 1,000-Hz sampling rate. The array

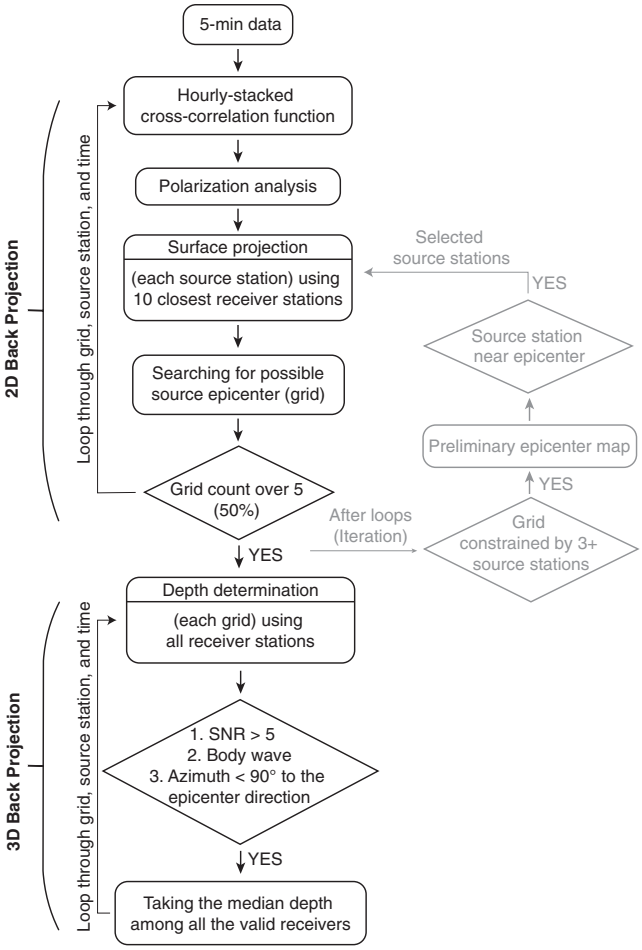

Figure 2. The workflow for the analyses in this study. The procedures in gray color are for source station selection and can be iterated multiple times. In this study, we perform two iterations to determine the virtual source station for each epicenter location.

aperture was ~250 m and the station spacing ranges from 15 to 35 m. During the experiment, a total of seven major eruptions of Steamboat occurred with six intervals varying between 3 and 8 days (Figure 1b). Because the analyses in this study are based on seismic interferometry and all the geophones use the same type of instrument, we did not remove the instrument response. In addition to seismic recording, the NPS placed pressure and temperature transducers in Cistern's pool located at ~3.5 m depth between July 11 and July 18 2019. Both *in situ* measurements were recorded at 1 min intervals. The continuous recordings were used to monitor the physical and thermal status of Cistern's pool during the Steamboat eruption cycle.

2.2. Distinct Hydrothermal Tremor From Steamboat and Cistern

From the seismographs recorded by the nearest stations, we observe clear cyclic low-frequency (1–5 Hz) seismic energy, hereafter called tremor, emitted from both Steamboat and Cistern (Figure 1b). The tremor amplitudes are higher prior to Steamboat's major eruptions and drop sharply afterward, which highly resembles the temporal variation of the 1–5 Hz tremors observed at Old Faithful Geyser (Wu et al., 2019). Different from the Old Faithful tremor, which intensified monotonically before each eruption, the amplitude variations of Steamboat and Cistern tremor are more variable. Between the two features, while the amplitude variations are clearly correlated on the first order, there are also distinct differences making the tremor signals from each of the features unique. For instance, both tremor amplitudes dropped sharply about the same time after the eruption on July 11. While amplitude recorded near Steamboat started to increase by the end of July 11, the recovery of amplitude near Cistern was delayed for about a half day (Figure 1b). This indicates that the recharge process is more complicated for the Steamboat–Cistern system (compared to a stand along geyser such as Old Faithful), possibly due to its intertwined plumbing structure. To study the architecture and the dynamics of Steamboat and Cistern, we explore the spatiotemporal pattern of the tremor origins below.

3. Methods

The distinct temporal patterns of tremor between Steamboat and Cistern demonstrate a multisource environment within the seismic array. Traditional source locating methods relying on arrival times and accurate velocity models (e.g., Gomberg et al., 1990; Guo et al., 2017; Kao & Shan, 2004; Richards et al., 2006) do not work for the observed hydrothermal tremor as no isolated event with a discernable arrival was observed and the shallow velocity structure is largely unknown. Moreover, as Steamboat and Cistern are only 100 m away, wavefield interference likely occurred persistently across the entire array. To probe the spatiotemporal pattern of the tremor in this study, we further develop an interferometry-based polarization analysis (Wu et al., 2019) to image the multisource migration of the Steamboat–Cistern tremor. The main workflow of the method is summarized in Figure 2 where the detailed description of each step is described in the following sections.

3.1. Seismic Interferometry

To enhance and isolate the 1–5 Hz tremor signals emitted within the Steamboat–Cistern system, we perform multicomponent cross-correlation. The cross-correlation method has the advantage of amplifying coherent signals observed at two stations where signals at different lag times represent signals originating from

different source locations. The method is particularly effective when a station is located close to a persistent tremor source. In such a case, the cross-correlation wavefield constructed using that station as the common station (or source station) and all other stations as receivers closely resembles the wavefield emitted by the tremor source but with a spontaneous excitation (Wu et al., 2017, 2019). Moreover, by preserving the relative amplitude between different components for each receiver, the particle motion and hence the polarization of the emitted wavefield can also be extracted using the three-component cross-correlation functions (CCFs; Lin et al., 2014; Wu et al., 2019). We note that the main focus of this study is to utilize the CCFs to investigate the tremor source. This is different from the common noise interferometry studies, which often focus on investigating wave propagation and subsurface velocity structure (e.g., Shapiro et al., 2005).

Adapting the process we implemented for Old Faithful Geyser (Wu et al., 2019), we first calculate the CCFs using 5-min nonoverlapping time windows, then perform temporal stacking to obtain 1-h CCFs. For each 5-min window, we cross-correlate the vertical component seismogram (Z) at a source station with all three-component seismograms (Z, E, and N) across the entire array. Thus, the CCFs are expressed as ZZ, ZE, and ZN or ZZ, ZR, and ZT after rotating to the radial (R) and transverse (T) directions. The relative amplitude information is preserved by applying the identical spectral and temporal normalizations to all components from the same time window (Bowden et al., 2015). For spectral normalization, we whiten the CCF spectrums by the 90th percentile averaged three-component spectrum across the entire array. For the temporal normalization, we first applied a Butterworth filter between 1 and 5 Hz to remove high-frequency energy; then all the filtered CCFs are normalized by the 90th percentile maximum amplitude of the vertical–vertical CCFs across the entire array. Note that the normalization process applied here is done one at a time for each source station. To obtain nonoverlapping 1-h CCFs, we linearly stacked the normalized 5-min CCFs. Here, we reference the 1-h CCFs based on the beginning time of each 1-h window.

Taking the station closest to Steamboat as the source, the CCFs 11 h before an eruption show a clear vertical–radial linear motion, indicative of a *P* wave, when the receiver is close (<40 m; Figure 3a). The wavefield converts to elliptical Rayleigh wave particle motions for distant receivers (>60 m; Figure 3c) while a hybrid motion is observed in the intermediate distance (~50 m; Figure 3b). Using the station closest to Cistern as the source, the CCFs with receivers close to Cistern also have clear *P* wave motions (e.g., Figure 3f), while the overall higher horizontal amplitude (ZR > ZZ) indicates that the tremor source is likely quite shallow. For receivers close to Steamboat, the presumed Cistern tremor signals however are overwhelmed and interfered by the Steamboat signals, as the dominant arrivals of CCFs lie within the negative lag time (Figures 3g and 3h). This indicates the Steamboat tremor is, in general, stronger compared to the Cistern tremor, which is also seen in the relative amplitudes depicted in Figure 1. In Sections 3.2 and 3.3, we will discuss how we only select the receivers close to the source station to investigate the tremor source location. In our following analyses, we automatically identify and characterize all tremor sources within the Steamboat–Cistern system by considering all stations across our array as possible source stations in addition to the stations that are closest to Steamboat and Cistern.

3.2. Polarization Analysis

Following the algorithm described by Jurkevics (1988), a polarization analysis is performed to determine the dominant direction of particle motion at each receiver station for a given source station. A $n \times 3$ matrix, $\boldsymbol{C} = \left[\boldsymbol{ZZ}, \boldsymbol{ZN}, \boldsymbol{ZE}\right]$, is first constructed using the three-component hourly stacked CCFs (ZZ, ZN, and ZE), where n is the number of time samples in the CCFs. To focus on tremor signals generated by sources closer to the source station, we only use CCFs between 0 and positive 1.5 s lag time. The 3×3 covariance matrix $\boldsymbol{S}$ can then be constructed as

$$\boldsymbol{S} = \frac{\boldsymbol{C}^T \boldsymbol{C}}{n}. \tag{1}$$

The eigenvalues $\left(\lambda_1, \lambda_2, \lambda_3\right)$ and the normalized eigenvectors $\left(\boldsymbol{u}_1, \boldsymbol{u}_2, \boldsymbol{u}_3\right)$ of $\boldsymbol{S}$ can be solved with the Singular Value Decomposition:

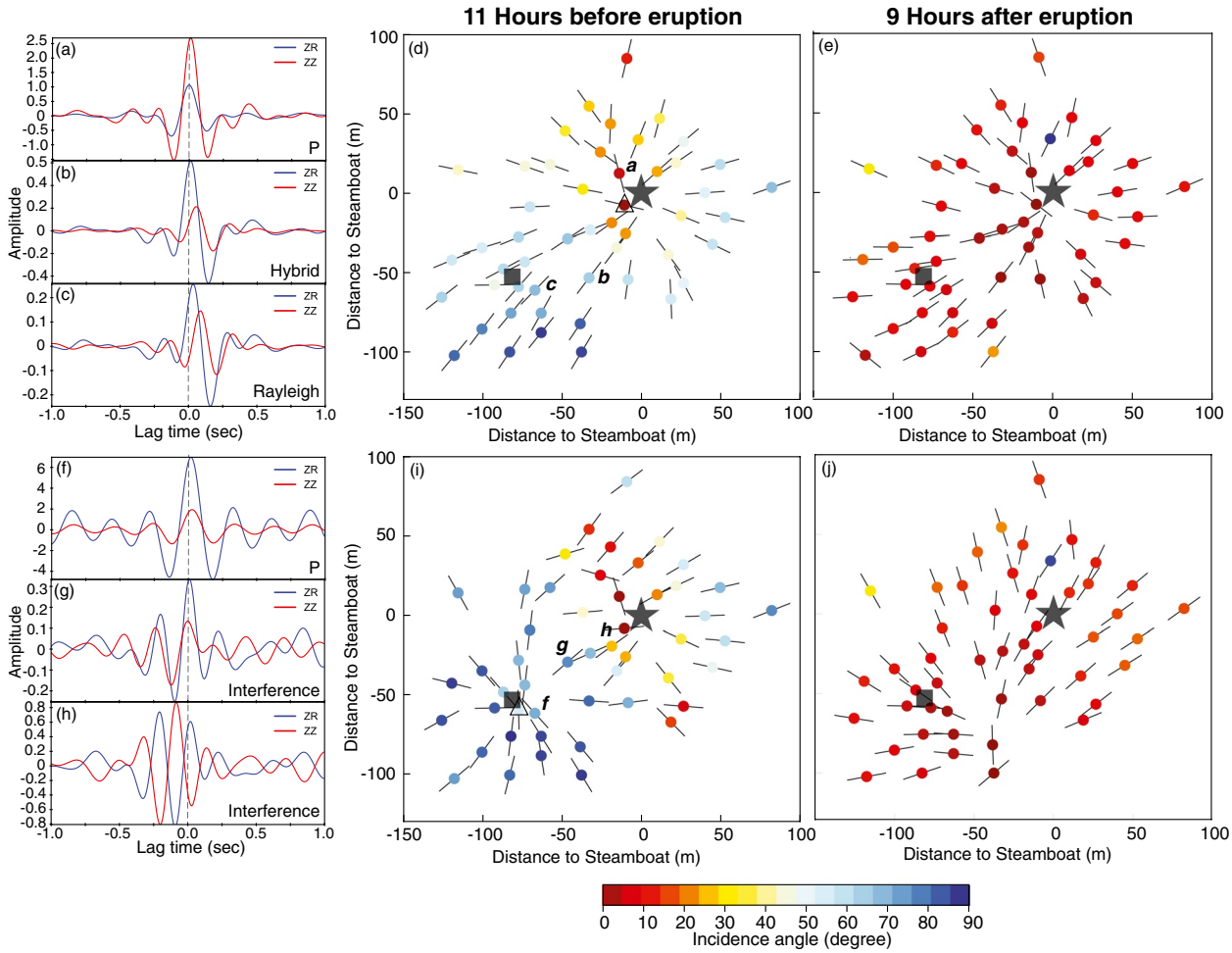

Figure 3. (a–c) Examples of vertical–vertical (ZZ) and vertical–radial (ZR) cross-correlations between a common source station (the open triangle denoted in (d)) and three different receiver stations (letters denoted in (d)). (d, e) Polarizations (bar: back azimuth direction; color: incidence angle) of multicomponent cross-correlations with a common source station (open triangle) near Steamboat 11 h before (d) and 9 h after (e) a major eruption. The black star and the black square denote Steamboat and Cistern locations, respectively. (f–h) Same as (a–c) but for a different common source station (the open triangle denoted in (i)) and three different example receiver stations (letters denoted in (i)). (i, j) Same as (d) and (e) but for a source station (open triangle) near Cistern.

$$\left(\boldsymbol{S}-\lambda_i \boldsymbol{I}\right)\boldsymbol{u}_i = \boldsymbol{0}, i = 1,2,3, \tag{2}$$

where $\boldsymbol{I}$ is the 3×3 identity matrix, $\boldsymbol{0}$ is the zero vector, and the eigenvalues are ordered as $\lambda_1 \geq \lambda_2 \geq \lambda_3$. The dominant polarized direction of the CCFs is the 3D eigenvector that corresponds to the largest eigenvalue, $\boldsymbol{u}_1 = \left(u_{Z\_1}, u_{N\_1}, u_{E\_1}\right)$. Based on $\boldsymbol{u}_1$, we obtain the azimuth $\left(\tan^{-1}\left(u_{N\_1} / u_{E\_1}\right)\right)$ and the incidence angle $\left(\cos^{-1}\left|u_{Z\_1}\right|\right)$, which we can use to identify and locate the hydrothermal tremor sources.

Example results of polarization analysis for source stations closest to Steamboat and Cistern are shown in Figure 3. Before the eruption, clear isotropic radiation patterns are observed for both source stations (Figures 3d and 3i) with the majority of receivers pointing toward Steamboat and Cistern, respectively, suggesting there are tremor sources beneath both features. For the source station near Cistern (Figure 3i), receivers nearby Steamboat are pointed toward Steamboat instead of Cistern suggesting Steamboat tremor is stronger and the cross-correlation signal in the negative lag interferes with the positive lag. When examining receivers close to the virtual sources, incidence angles near Cistern (Figure 3i) are overall larger compared to Steamboat (Figure 3d) suggesting that the Cistern source is closer to the surface. We note that this apparent depth discrepancy could somewhat be offset by the elevation difference between the two features, where Cistern is about 10 m lower than Steamboat in elevation. After the eruption, clear isotropic

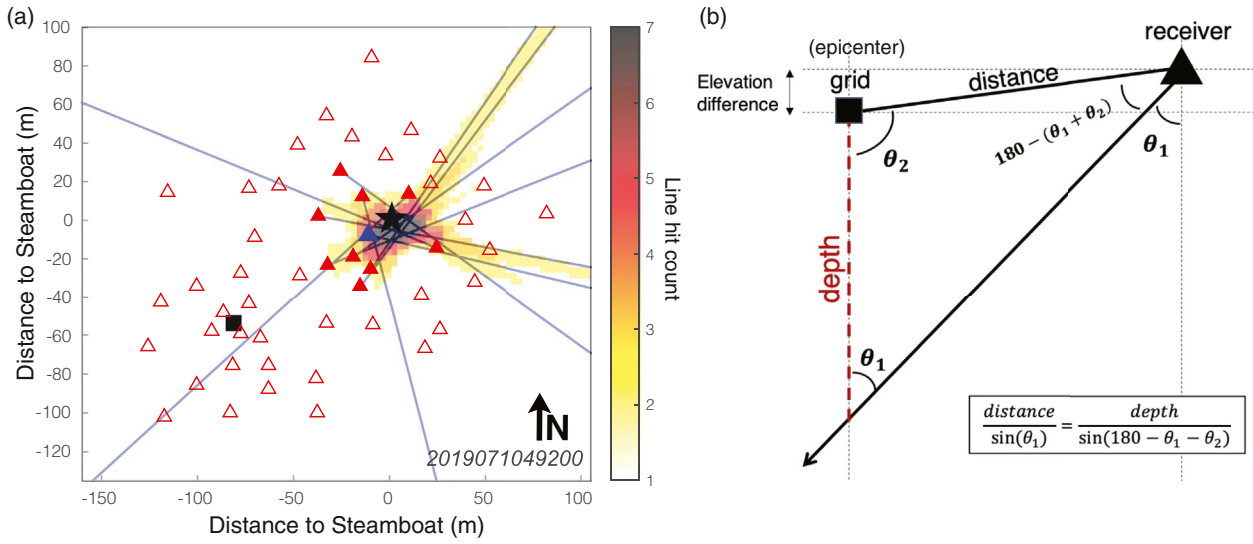

Figure 4. (a) An example of 2D surface back projection of the polarization analysis using 10 closest receiver stations (red-filled triangle) for a given source station (blue triangle). Each line illustrates the azimuth measured at each receiver station from the polarization analysis. The color-coded contours represent the hit count of the projected lines. The epicenters (grid points) with line hit count over 5 will be saved for further depth determination. The black star and square mark the Steamboat and Cistern locations, respectively. (b) Depth determination accounting for the elevation difference based on the trigonometric relationship marked in the lower-right box. θ_1 is the incidence angle constrained by polarization analysis at a receiver station and θ_2 is the incidence angle of the grid-receiver vector.

radiation patterns are again observed for the two source stations although the smaller overall incidence angles indicate the deepening of the sources (Figures 3e and 3j). Moreover, the center of the radiation pattern, the presumed source location, shifts about 60 m toward the southeast for the Cistern case. To determine the spatiotemporal distribution of the tremor sources, we propose a two-step back projection process to progressively determine the source distribution first in 2D and then in 3D.

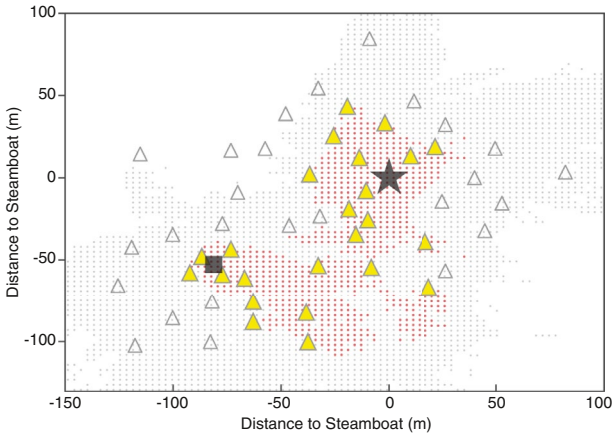

Figure 5. The map of the potential tremor epicenters from the first iteration of the 2D back projection. The gray and red dots are the epicenters located by at least one and three source stations, respectively. The selected source stations for the second iteration are marked as yellow triangles. The black star and square mark the Steamboat and Cistern locations, respectively.

3.3. Surface Back Projection (2D)

Instead of a direct 3D back projection, for each source station, we first use the 10 closest receiver stations to detect and locate the epicenter of the tremor sources in 2D space. Using only the closest receivers avoids potential interference from other sources and is effective in identifying all potential tremor sources regardless of their strength. We create a 2D Cartesian coordinate grid with 3-m spacing for the whole area, with each grid point representing a possible epicenter of the tremor source location. The azimuth measured at each receiver from the polarization analysis is projected as an infinite ray on the 2D surface (Figure 4a). Note that we resolve the 180° ambiguity of the ray direction by assuming a downgoing direction of the eigenvector $\boldsymbol{u}_1$ (i.e., $u_{Z\_1} < 0$) as the presumed sources should be located beneath the surface. The orthonormal distance between each grid and the raypath can thus be calculated. For each grid point, we determine the number of raypaths with an orthonormal distance smaller than 8 m. When that number is higher than 50% (five hits), we consider the grid point as a possible tremor epicenter.

A robust tremor epicenter should be inferred by multiple source stations nearby, and we remove all epicenter grid points inferred by only one or two source stations independent of time from further analysis (Figure 5). As our interferometry method works best when source stations are close to the tremor epicenters, we then further remove source stations that are

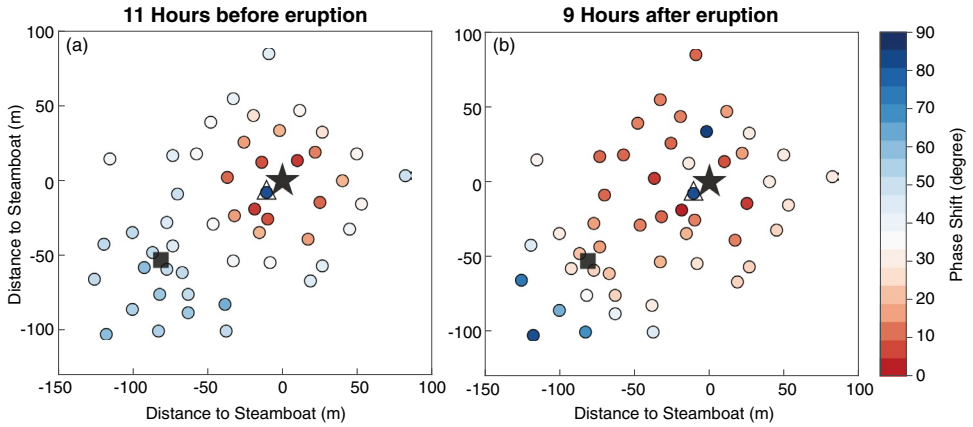

Figure 6. Measured phase shift between ZZ and ZR components of the cross-correlation functions around (a) 11 h before and (b) 9 h after the eruption. The common source station is denoted by the open triangle. We define *P* wave like motion as having a phase shift smaller than 30°. The black star and square represent Steamboat and Cistern locations, respectively.

5 m away from the refined epicenter locations (Figure 5). This epicenter and station selection process can be iterative and is marked as gray procedures in Figure 2. Note that we use a finer grid spacing (1 m) in our second iteration before proceeding to the 3D back projection process discussed below.

3.4. Depth Back Projection (3D)

A large array aperture is important for accurate source depth determination as the depth can be better constrained with a wide range of incidence angles. Only *P* wave particle motion is useful, however, as the incidence angle of a Rayleigh wave will always be more or less horizontal. To determine the source depth, for each source station and each possible epicenter inferred by that source station, we include all receivers with reliable *P* wave like motion. Here, we define *P* wave like motion if the phase shift between the vertical and radial components of the CCFs is smaller than 30° (e.g., Figure 6). To preclude receivers with signals potentially interfered by other sources, we impose a signal-to-noise ratio threshold of 5 on ZZ and require the azimuthal angle to be within 90° of the source epicenter. The signal-to-noise ratio is defined as the ratio between the peak amplitude within the signal window (0–2 s) and the root-mean-square energy within the noise window (2–4 s). For each receiver passing the selection criteria above, assuming a homogenous velocity model, the incidence angle is then used to determine the source depth with topography accounted for based on the following trigonometric relationship:

$$\frac{\text{distance}}{\sin\left(\theta_1\right)} = \frac{\text{depth}}{\sin\left(180 - \theta_1 - \theta_2\right)}, \tag{3}$$

where the distance is the 3D distance between the epicenter grid and the receiver, θ_1 is the incidence angle, θ_2 is the incidence angle of the grid-receiver vector (Figure 4b). The elevation is taken from the high-resolution (0.5 m) Lidar data acquired from OpenTopography (ISB, 2009).

Note that spatial velocity variations can potentially distort the raypath and affect the observed incident angle on the surface. We consider Equation 3 a reasonable first-order approximation, given the relatively long-wavelength (~330 m assuming a 1 km/s *P* wave velocity) of the 1–5 Hz seismic energy (compared to the depth we are investigating). We also note that downgoing *P* and *SV* waves originated from the free surface should be considered to correct for the difference between the upgoing *P* wave incident angle and the apparent incident angle on the surface (Park & Ishii, 2018). Further improvement of our result hence could be obtained with the availability of a high spatial resolution velocity model in the area, although that is out of the scope of the current study. For each epicenter and a corresponding source station, we take the median depth among all the depths inferred by all qualified receivers as the preliminary resolved depth. Then, we

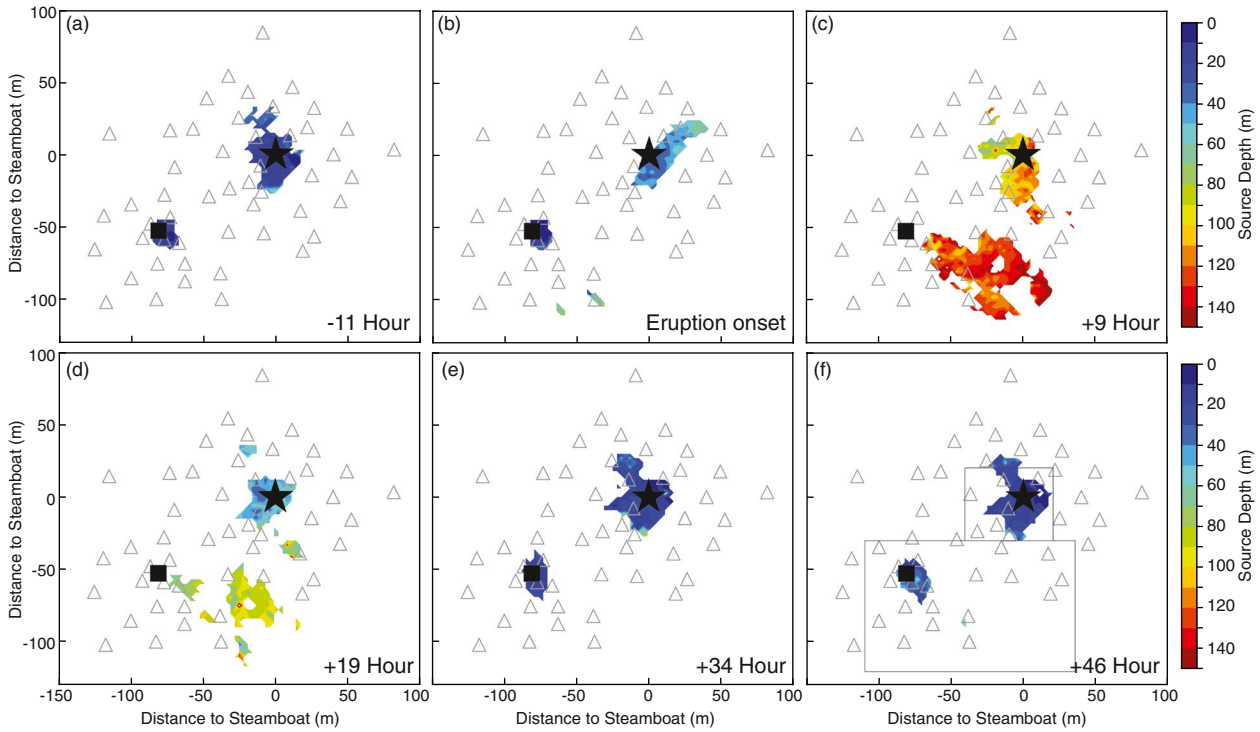

Figure 7. The tremor source locations color coded by the estimated depth. (a–f) The six different times during the eruption/recharge cycle relative to the eruption on July 11 2019. The two open rectangles in (f) mark the areas for the averaged depth calculation shown in Figure 9. The black star and square represent Steamboat and Cistern locations, respectively.

take the median depth of the preliminary depths from different source stations as the best estimation of the source depth for that grid (Figure 7).

4. Results

4.1. Spatiotemporal Distribution of the Tremor

By performing the polarization and back projection analyses for all the 1-h CCFs, we observed systematic tremor source migration within the Steamboat–Cistern system throughout the eruption cycles. Taking the eruption on July 11, 2019 as an example (Figure 7), around 11 h before the eruption, the Steamboat and Cistern tremor sources were at ~25 and ~15 m depth, respectively. At the onset of the eruption, the Steamboat tremor began to deepen while the Cistern tremor remained at the same level. Nine hours after the eruption, both tremor sources decreased to the deepest depths, with the Steamboat tremor slightly shallower (~120 m) than Cistern tremor (~140 m). Approximately, 34 h after the eruption, both tremor sources returned to shallow depths and stayed shallow until the next eruption. Throughout the eruption cycle, the Steamboat tremor epicenters were persistently confined near the surficial vent indicating a near vertical conduit. While persistent tremor sources are also observed directly beneath Cistern's pool before the eruption, a considerable lateral shift is observed between 2 and approximate 30 h after the eruption. This deep, laterally shifted, wide-spread area indicates a lateral turn and widening of the Cistern plumbing structure at depth.

4.2. Plumbing Architecture Outline

If we assume the tremor originates from the steam/liquid phase transition within the water column, the outline of all the possible tremor sources in 3D, independent of time, illuminates the extent of the plumbing architecture. Here, to only illustrate the most robust 3D plumbing features, we create 3D isosurface plots (Figure 8) using a stricter than standard tremor source selection criterion (i.e., with at least 80% hit count

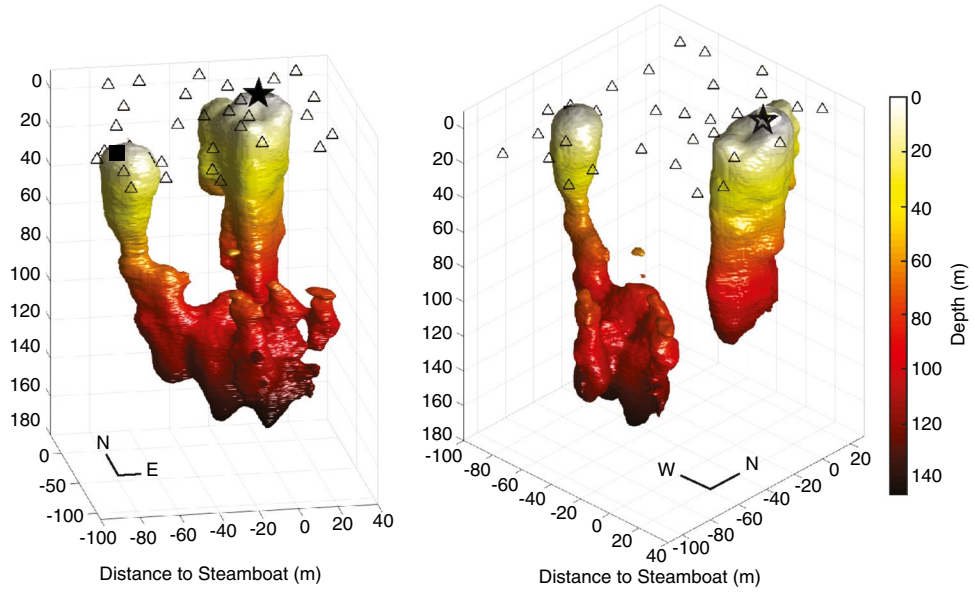

Figure 8. The outline of the Steamboat and Cistern plumbing systems with two viewing angles, inferred based on the isosurface of the tremor source locations throughout the entire recorded cycles. The structure, color-coded by the depth, delineates the observed seismically active area during the eruption cycles. The solid star, solid square, and open triangles denote Steamboat, Cistern, and station locations on the surface, respectively.

instead of 50% during the surface projection analysis described in Section 3.3). While the fine-scale structure is likely obscured by the intrinsic resolution limit imposed by our array configuration and uncertainty associated with the subsurface velocity structure, the 3D model nevertheless allows us to visualize the Steamboat–Cistern subsurface plumbing complex for the first time. In particular, Figure 8 illustrates that the plumbing geometry beneath Steamboat is approximately vertical and extends to at least ~120 m depth. The plumbing conduit beneath Cistern is vertical from the surface to ~65 m depth. The bottom of the vertical conduit is laterally connected to a reservoir between ~80 and at least ~140 m depth through an oblique and elongated conduit between ~65 and ~100 m depth. The center of the reservoir is ~60 m southeast of Cistern's surface pool. Based on the structural continuity, hereafter we refer to Cistern's plumbing to be the system as a whole, including the offset reservoir. Despite the fact that we know Cistern and Steamboat are hydrologically connected, we do not observe any overlapping between their tremor sources in space down to ~140 m depth. We hypothesize that the connection is likely aseismic and/or is deeper than the resolution limit imposed by the network aperture. It must be noted that the lateral dimension of the structure depicted in Figure 8 is sensitive to the 80% selection criterion we choose and should be interpreted carefully, particularly considering the limited resolution.

4.3. Distinct Recharge Evolution Patterns

As the observed hydrothermal tremor was excited by the liquid/gas phase transition, the ability to image the migration of the tremor sources hence allows us to track the phase-transition horizons of the Steamboat–Cistern system throughout the eruption cycles. From Figure 7, we can see the tremor sources are somewhat clustered for both Steamboat and Cistern. To find the centroid of the clusters, we first manually choose the source areas for Steamboat and Cistern (the open rectangles in Figure 7). For each time (hourly window) and within each source area, we perform a grid search to find a circle (with a 15-m radius) that contains the most abundant tremor source locations. We then determine the depth based on the averaged depth of the tremor sources within the resultant circle. Given the depth, in conjunction with the plumbing outline (Figure 8), we can reproduce the complete recharge evolution of Steamboat and Cistern throughout the six eruption cycles (Figure 9). Because the interval between eruptions (IBEs) varied significantly (3–8 days) during our data time period, here we summarize the general features that are common to all eruptions.

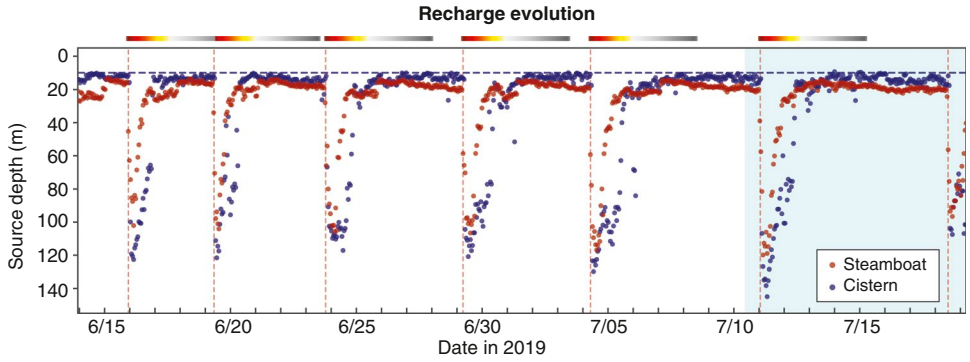

Figure 9. The temporal depth variation of Steamboat (red dots) and Cistern (blue dots) tremor sources. The source depth is relative to Steamboat's elevation and the horizontal blue-dashed line represents the ground surface level of Cistern. The vertical red-dashed lines mark the Steamboat eruption times. The light blue area represents the time period shown in Figure 11. The top colored lines represent the time after eruption corresponding to the exact time window and color shown in Figure 10.

Prior to eruptions, the phase-transition horizon was predominantly at ~25 m depth beneath Steamboat. Although it was at ~15 m depth (relative to Steamboat vent), the phase-transition horizon beneath Cistern was in fact much closer to the surface (<5 m) as Cistern is ~10 m lower than the reference Steamboat elevation. Immediately after each eruption, the phase-transition horizon at Steamboat dropped vertically in response to heat and water evacuation and potential cold water refill through a permeable medium (Munoz-Saez, Namiki, et al., 2015) or to condensed steam flowing back to the conduit (Hutchinson et al., 1997). In contrast, the phase-transition horizon at Cistern does not drop until 1–2 h later. About ~5–9 h after each eruption, the phase-transition horizons at both Steamboat and Cistern reached the greatest depth (>100 m) within the vertically elongated conduit and the offset reservoir, respectively. Note that at this time the water phase (<60 min) of the eruption had ceased (White et al., 1988). After that, the phase-transition horizons at Steamboat and Cistern both quickly ascended along the inferred plumbing structures (Figure 8) and then slowed down when reaching 10–30 m depth. During the migration, the phase-transition horizon at Steamboat was consistently shallower and reached the 10–30 m level hours earlier than Cistern. Finally, both phase-transition horizons remained at shallow depths for days until the systems become primed for another eruption.

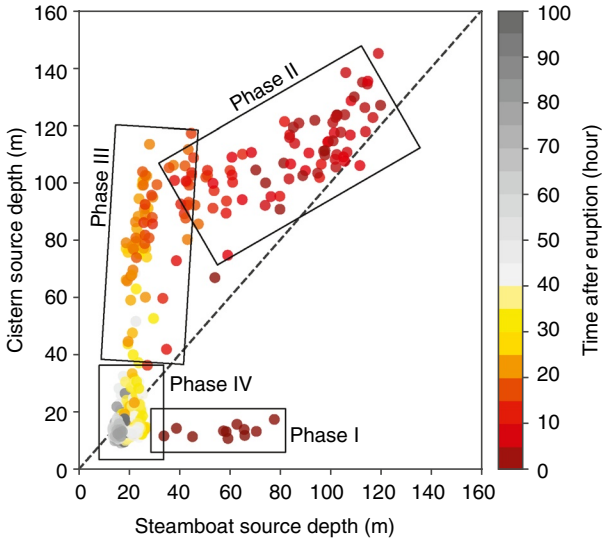

Figure 10. The depth relationship between the Steamboat and Cistern tremor source locations throughout the entire recorded period color-coded by the time after eruptions. The four phases (I–IV) highlight the distinct characteristic of different depth migration rates for Steamboat and Cistern tremor sources. As a reference, the diagonal gray-dashed line marks the equal depth.

5. Discussion

5.1. Contrasting Tremor Migration Rate Between Steamboat and Cistern

From the recharge evolution shown in Figure 9, we observe that Steamboat and Cistern have distinct but related recharge progressions. To further quantify the interaction between the two, we highlight four phases during the recharge that have distinct tremor migration rates for Steamboat and Cistern (Figure 10). Phase I: at the onset of Steamboat's major eruptions, the Steamboat tremor drops immediately, while Cistern tremor remains stagnant at surface level for 1–2 h before dropping to deeper depths. Phase II: in the first 20 h after an eruption, the Steamboat tremor migrates upward at rates of more than 2 times faster than Cistern. Phase III: between 20 and 30 h after an eruption, Cistern's tremor migration rate is an order of magnitude faster than Steamboat and is 3–4 times faster than it was in the first 20 h. Phase IV: after 30–40 h posteruption, both tremor sources return to shallower depths (~10–30 m deep) and stay at similar levels for days until the next eruption.

Assuming the heat influx is constant, the observed migration rate variation may indicate changes in plumbing dimensions from deep to shallow, as heat can accumulate faster within a narrower plumbing structure. For Cistern, the slow migration rate between 140 and 90 m depth during Phase II likely reflects a large and expanded structure consistent with the wide-spread tremor source area observed (Figures 7c and 8). The subsequent faster migration rates (Phase III) thus corresponds to the narrowing of the Cistern plumbing structure, which turns into a narrower vertical conduit between ~90 and ~20 m beneath Cistern (Figure 8). In Phase IV, the Cistern migration rate slowed down considerably above ~20 m depth and eventually became stagnant when nearly reaching the surface. At this shallow depth, the Cistern conduit gradually widens toward the surface pool, and the heat influx from depth and heat diffusion at the pool surface are likely close to equivalent. For Steamboat's plumbing, the fast migration rate in Phase II between 120 and 30 m depth likely suggests a vertical conduit that is much smaller in size compared to the Cistern reservoir (Figure 8). It is unclear why Steamboat tremor sources stay at 20–30 m depth for days prior to the eruption (Phase IV). This depth might be somehow controlled by the elevation difference between Steamboat and Cistern but we cannot rule out the existence of a shallow reservoir or a bubble trap feature that enables two-phase mixture (Vandemeulebrouck et al., 2014). Note that this 20–30 m tremor depth before eruptions is slightly deeper than the ~20 m depth observed at Old Faithful (Wu et al., 2019), which might cause the greater heights of Steamboat eruptions (Reed et al., 2021).

5.2. Comparison With *In Situ* Pressure and Temperature Data

It is still enigmatic why Cistern has a late response (Phase I) to a major eruption of Steamboat and how these two systems are connected. With the availability of the *in situ* pressure and temperature measurements placed within Cistern's pool (~3.5 m depth), we can better understand how Cistern relates to Steamboat by closely comparing the physical state of Cistern with the tremor evolution (Figure 11). At the onset of eruption, temperature at Cistern's pool dropped (less than a half degree [°C]) immediately but the water level was steady and kept boiling for 1–2 h, consistent with the observed shallow Cistern tremor depth during Phase I (Figures 7b and 10). This apparent delay in response for Cistern to Steamboat eruptions indicates that the two features might not connect through an open structure but perhaps through a diffusive porous medium (Ingebritsen & Rojstaczer, 1993; Munoz-Saez, Namiki, et al., 2015), where the permeable flow is driven by the hydrostatic pressure gradient. The immediate temperature decrease is likely the result of immediate reduction of heat influx from deep resulting from Steamboat's major eruption.

About 1–2 h after eruption onset, the water level at Cistern's pool gradually drops and takes ~20 h to drop >3.5 m (below the transducer). Around this time, Steamboat tremor raises to about 30 m depth coinciding with the tremor amplitude increase observed at the surface. Intriguingly, this time coincides with the oscillation of Cistern tremor and the spontaneous increase in Cistern seismic amplitude. Around 10 h later (30 h after eruption), the water at Cistern gradually refills surpassing the 3.5 m level and starts to boil at ~2 m level a few hours later. The boiling is consistent with both the migration of Cistern tremor to a shallower depth and the increase tremor amplitude at the surface (Figure 11d). Around 45 h after the eruption, a sudden decrease in Cistern seismic amplitude that corresponds to the drops of both tremor depth and the water temperature is observed. Note that the pressure data consistently indicate water disturbance (boiling) while the temperature has dropped below the boiling temperature (93°C), suggesting Cistern's pool was thermally stratified and the boiling is occurring somewhere deeper than the transducer. Overall, the observed tremor migration and amplitude at Cistern are remarkably consistent with the appearance of water level and the boiling status within Cistern's pool. Around 55 h posteruption, Cistern is completely refilled and overflowing until the next major eruption, with no clear change in the physical state related to Steamboat's minor eruption activity (black-dashed line in Figure 11). Steamboat's minor eruptions are typically water outflow events and splashes of water up to 30–50 ft and the timing is determined from a temperature logger in Steamboat's run-off channel installed by NPS.

The delay of tremor migration (both descending and ascending) combined with the insensitivity of Cistern to Steamboat's minor eruptions again indicates that the two features are probably not connected through an open channel that fluid can circulate freely. On the other hand, no significant Steamboat tremor depth variation has been observed corresponding to the resumption of minor eruptive activity. This suggests the minor eruptions are mostly controlled by shallow dynamic processes and do not involve the deeper part of

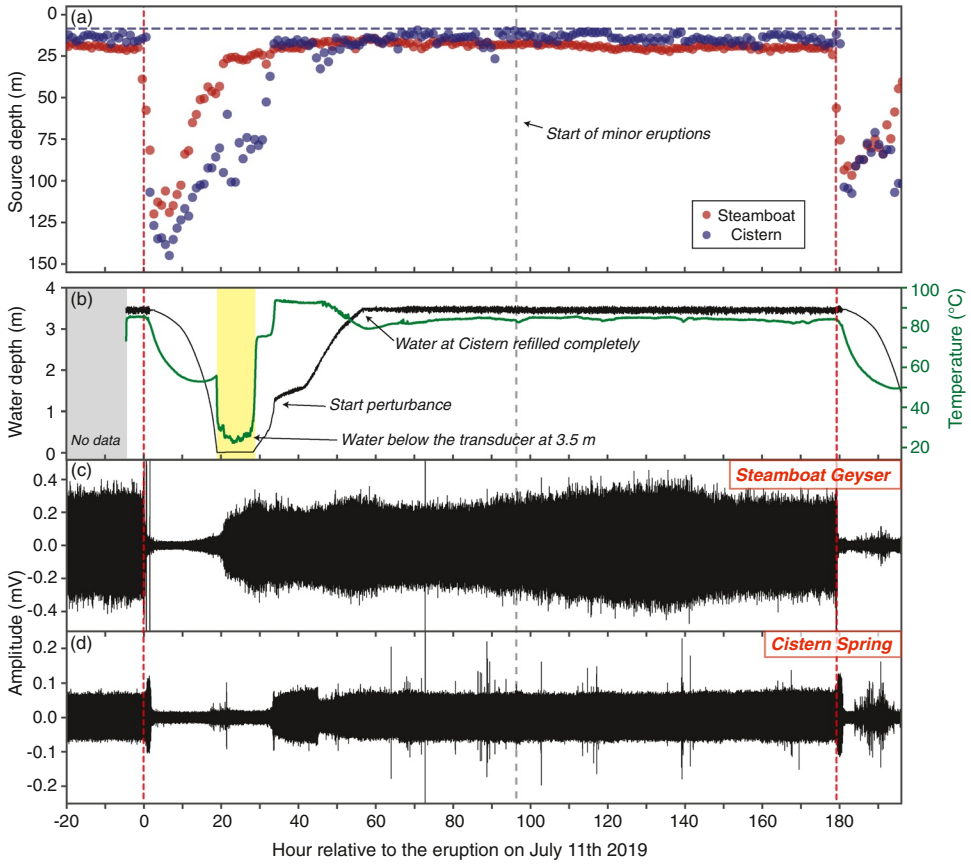

Figure 11. (a) Comparison between tremor depths, (b) *in situ* water level (black) and temperature (green) measurements at 3.5 m depth within Cistern's pool, and (c, d) the 1–5 Hz tremor amplitudes observed near Steamboat and Cistern for the Steamboat eruption cycle on July 11 2019 (light blue time window in Figure 9). The red-dashed lines mark the eruption times. The gray and yellow areas mark the time windows when the *in situ* data are not available and water level dropped below the transducer, respectively.

the plumbing system. Further thermal dynamic modeling will be needed to provide more insights into the interaction between Steamboat and Cistern as well as the eruption dynamics of the Steamboat system. That is, however, beyond the scope of this current study.

5.3. Steamboat's Predictability?

Steamboat is an episodic but not periodic geyser. During the current active phase since March 2018, the IBE has changed by an order of magnitude from 3 to 35 days. It is interesting and enigmatic, whether Steamboat eruptions are stochastic or deterministic, and if deterministic, whether Steamboat eruptions can be predicted. For a predictable geyser such as Old Faithful, its periodic eruptions are considered an outcome of thermodynamic equilibrium, where the minor errors (10%–15% of the eruption interval) may come from a stochastic component. Like Old Faithful, previous geyser prediction schemes are developed based on periodicity of the surface activity (Eibl et al., 2020; Gouveia & Friedmann, 2006). To the best of our knowledge, no prediction has ever been attempted on "nonregular" geysers such as Steamboat. Therefore, using the nodal data, we could first explore the geyser predictability via its internal behavior. One caveat is that the nodal deployment was restricted by battery power so that only six eruption cycles are recorded as Steamboat has overall longer time scales (hours to days) for its recharge and eruptive activity compared to other studied periodic geysers (seconds to minutes; e.g., Eibl et al., 2020; Munoz-Saez, Manga, et al., 2015; Munoz-Saez, Namiki, et al., 2015; Rinehart, 1965). Nevertheless, the recorded IBE varied significantly from 3 to 8 days, which, we consider could be a good proxy as a pilot study.

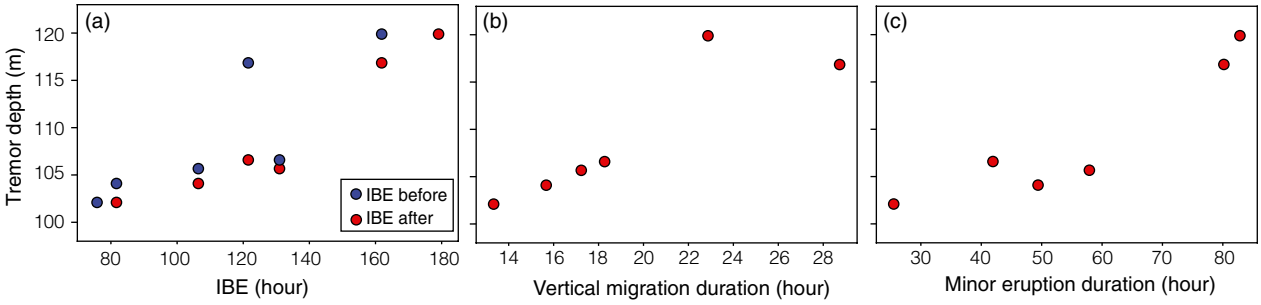

Figure 12. The relationship between the deepest tremor depth after the eruption and (a) the interval between eruption (IBE), (b) the vertical migration durations from the deepest depth to shallow, and (c) minor eruption duration. The IBE before and after represent the intervals to the previous and the next eruption, respectively.

From the recharge evolution, we observe a positive relationship between the deepest tremor depth and the IBEs (Figure 12a). The variation of the deepest tremor depth can be attributed to the various amount of energy evacuated from eruptions, hence the correlation with IBEs may suggest that Steamboat's system has a steady heat influx, and the eruptions are due to the outcome of equilibrium. Interestingly, there are two parameters positively correlated with the deepest tremor depth: the time duration for tremor migration from deepest depth to shallow and the minor eruption duration (Figures 12b and 12c). Both time durations increased when the tremor was deeper. The longer migration time is reasonable considering a steady heat influx, and we speculate the minor eruption duration is modulated by the waiting time for the shallow reservoir to be sufficiently heated and primed for an eruption (Namiki et al., 2016). Because the 1–5 Hz seismic amplitude increases sharply when the tremor returns to shallower depths (Figure 11c), data from a single station may offer sufficient information for prediction and collecting continuous data successively over a long time period might be feasible. Combining the minor eruption time, it may be possible to statistically evaluate Steamboat's predictability, which will be the subject of future studies.

6. Conclusion

To understand the underground architecture and the eruption/recharge dynamics of Steamboat Geyser and Cistern Spring, we deployed a dense three-component nodal array in the vicinity of Steamboat and Cistern between June and July 2019. From the continuous recordings, we observed distinct low-frequency hydrothermal tremors excited by liquid/gas phase transition within both Cistern and Steamboat. The tremor is clearly associated with Steamboat's eruption cycle and showed no isolated events or discernable arrivals. To constrain the spatiotemporal location of the tremor, we developed a new method that combines multicomponent cross-correlation, polarization analysis, and 2D then 3D progressive back projections. Results of mapping the 3D tremor source locations successfully outline Steamboat and Cistern's plumbing structure down to 140 m depth. Steamboat's plumbing is approximately vertical and extends to at least ~120 m depth. The conduit beneath Cistern is vertical from the surface to ~65 m then connected to a large and laterally offset reservoir down to ~140 m depth through an oblique conduit. Seismically, we observe no clear physical connections between Steamboat and Cistern. Tracking the depth horizon of the tremor migration, we reveal the recharge evolution and interaction of Steamboat and Cistern throughout the eruption cycles with hourly resolution. Tremor sources within both features dropped to depths >100 m after the eruption and tremor sources gradually shallowed following the warming of the systems, then stayed at shallow levels for days until the next eruption. The exact depths and the migration rates are distinct, however, for Steamboat and Cistern indicating the two systems are likely connected through a porous medium instead of open channels. Future hydrothermal modeling and data collection may provide insights into the fluid/energy transmission within the porous medium and the spatial extent of the hydrothermal impact in response to Steamboat's activity.

Data Availability Statement

The data (Farrell & Lin, 2019) used in this study are available at IRIS DMC (https://doi.org/10.7914/SN/9N_2019).

Acknowledgments
The authors thank Michael Manga for insightful discussions and initial review. In addition, we appreciate constructive reviews by Michael Bostock, Phil Dawson, Alicia Hotovec-Ellis, and the anonymous associate editor. Data collection was performed under Yellowstone National Park permit YELL-2019-SCI-8058, and YNP permit 2016-9. We would like to thank Behnaz Hosseini and Mariah Radue for help during the field deployment and Annie Carlson in the Yellowstone Center for Resources for help in the permitting process. This research is supported by NSF EAR-1753362.

References

Adelstein, E., Tran, A., Saez, C. M., Shteinberg, A., & Manga, M. (2014). Geyser preplay and eruption in a laboratory model with a bubble trap. *Journal of Volcanology and Geothermal Research*, *285*, 129–135.

Ardid, A., Vera, E., Kelly, C., Manga, M., Munoz-Saez, C., Maksymowicz, A., & Ortega-Culaciati, F. (2019). Geometry of geyser plumbing inferred from ground deformation. *Journal of Geophysical Research: Solid Earth*, *124*, 1072–1083. https://doi.org/10.1029/2018JB016454

Belousov, A., Belousova, M., & Nechayev, A. (2013). Video observations inside conduits of erupting geysers in Kamchatka, Russia, and their geological framework: Implications for the geyser mechanism. *Geology*, *41*(4), 387–390.

Bowden, D. C., Tsai, V. C., & Lin, F. C. (2015). Site amplification, attenuation, and scattering from noise correlation amplitudes across a dense array in Long Beach, CA. *Geophysical Research Letters*, *42*, 1360–1367. https://doi.org/10.1002/2014GL062662

Carr, B., Sims, K. W., Ciraula, D., & Bouligand, C. (2019). What does Old Faithful look like below the surface and why is it there? New hydrogeophysical and time-lapse imaging of Old Faithful, Yellowstone National Park. *AGU Fall Meeting Abstracts*. V24B-02.

Caylor, J. R. (2020). Shallow seismic modeling of the hydrothermal plumbing system beneath Old Faithful Geyser in the Upper Geyser Basin of Yellowstone National Park. *Open Access Theses & Dissertations*. 2945. https://scholarworks.utep.edu/open_etd/2945

Eibl, E. P. S., Hainzl, S., Vesely, N. I. K., Walter, T. R., Jousset, P., Hersir, G. P., & Dahm, T. (2020). Eruption interval monitoring at Strokkur Geyser, Iceland. *Geophysical Research Letters*, *47*, e2019GL085266. https://doi.org/10.1029/2019GL085266

Farrell, J., & Lin, F.-C. (2018). *Steamboat geyser nodal experiment 2018 [Data set]*. International Federation of Digital Seismograph Networks. https://doi.org/10.7914/SN/8N_2018

Farrell, J., & Lin, F.-C. (2019). *Steamboat geyser nodal experiment 2019 [Data set]*. International Federation of Digital Seismograph Networks. https://doi.org/10.7914/SN/9N_2019

GeyserTimes. (2020). *Eruptions of Steamboat geyser 2018–2020* [online database]. Available from http://www.geysertimes.org/archive/

Gomberg, J. S., Shedlock, K. M., & Roecker, S. W. (1990). The effect of S-wave arrival times on the accuracy of hypocenter estimation. *Bulletin of the Seismological Society of America*, *80*(6A), 1605–1628.

Gouveia, F. J., & Friedmann, S. J. (2006). *Timing and prediction of CO_2 eruptions from crystal geyser, UT (No. UCRL-TR-221731)*. Livermore, CA: Lawrence Livermore National Lab. (LLNL).

Guo, H., Zhang, H., Nadeau, R. M., & Peng, Z. (2017). High-resolution deep tectonic tremor locations beneath the San Andreas Fault near Cholame, California, using the double-pair double-difference location method. *Journal of Geophysical Research: Solid Earth*, *122*, 3062–3075. https://doi.org/10.1002/2016JB013919

Hurwitz, S., & Manga, M. (2017). The fascinating and complex dynamics of geyser eruptions. *Annual Review of Earth and Planetary Sciences*, *45*(1), 31–59. https://doi.org/10.1146/annurev-earth-063016-015605

Hutchinson, R. A., Westphal, J. A., & Kieffer, S. W. (1997). In situ observations of Old Faithful geyser. *Geology*, *25*(10), 875–878.

Ingebritsen, S. E., & Rojstaczer, S. A. (1993). Controls on geyser periodicity. *Science*, *262*(5135), 889–892.

ISB. (2009). EarthScope Intermountain Seismic Belt LiDAR Project. NCALM, UNAVCO, EarthScope, and National Science Foundation. distributed by OpenTopography. https://doi.org/10.5069/G9VD6WCS

Jurkevics, A. (1988). Polarization analysis of three-component array data. *Bulletin of the Seismological Society of America*, *78*(5), 1725–1743.

Kao, H., & Shan, S.-J. (2004). The source-scanning algorithm: Mapping the distribution of seismic sources in time and space. *Geophysical Journal International*, *157*(2), 589–594.

Karlstrom, L., Hurwitz, S., Sohn, R., Vandemeulebrouck, J., Murphy, F., Rudolph, M. L., et al. (2013). Eruptions at Lone Star Geyser, Yellowstone National Park, USA: 1. Energetics and eruption dynamics. *Journal of Geophysical Research: Solid Earth*, *118*, 4048–4062. https://doi.org/10.1002/jgrb.50251

Kedar, S., Kanamori, H., & Sturtevant, B. (1998). Bubble collapse as the source of tremor at Old Faithful Geyser. *Journal of Geophysical Research*, *103*(B10), 24283–24299.

Kedar, S., Sturtevant, B., & Kanamori, H. (1996). The origin of harmonic tremor at Old Faithful Geyser. *Nature*, *379*(6567), 708–711.

Kieffer, S. W. (1984). Seismicity at Old Faithful Geyser: An isolated source of geothermal noise and possible analogue of volcanic seismicity. *Journal of Volcanology and Geothermal Research*, *22*(1–2), 59–95.

Kieffer, S. W. (1989). Geologic nozzles. *Reviews of Geophysics*, *27*(1), 3–38.

Lin, F.-C., Tsai, V. C., & Schmandt, B. (2014). 3-D crustal structure of the western United States: Application of Rayleigh-wave ellipticity extracted from noise cross-correlations. *Geophysical Journal International*, *198*(2), 656–670.

Lynne, B. Y., Heasler, H., Jaworowski, C., Smith, G. J., Smith, I. J., & Foley, D. (2018). Ground penetrating radar documents short-term near-surface hydrological changes around Old Faithful Geyser, Yellowstone National Park, USA. *Journal of Volcanology and Geothermal Research*, *354*, 1–12.

Munoz-Saez, C., Manga, M., Hurwitz, S., Rudolph, M. L., Namiki, A., & Wang, C.-Y. (2015). Dynamics within geyser conduits, and sensitivity to environmental perturbations: Insights from a periodic geyser in the El Tatio geyser field, Atacama Desert, Chile. *Journal of Volcanology and Geothermal Research*, *292*, 41–55. https://doi.org/10.1016/j.jvolgeores.2015.01.002

Munoz-Saez, C., Namiki, A., & Manga, M. (2015). Geyser eruption intervals and interactions: Examples from El Tatio, Atacama, Chile. *Journal of Geophysical Research: Solid Earth*, *120*, 7490–7507. https://doi.org/10.1002/2015JB012364

Namiki, A., Ueno, Y., Hurwitz, S., Manga, M., Munoz-Saez, C., & Murphy, F. (2016). An experimental study of the role of subsurface plumbing on geothermal discharge. *Geochemistry, Geophysics, Geosystems*, *17*, 3691–3716. https://doi.org/10.1002/2016GC006472

Nayak, A., Manga, M., Hurwitz, S., Namiki, A., & Dawson, P. B. (2020). Origin and properties of hydrothermal tremor at Lone Star Geyser, Yellowstone National Park, USA. *Journal of Geophysical Research: Solid Earth*, *125*, e2020JB019711. https://doi.org/10.1029/2020JB019711

Park, S., & Ishii, M. (2018). Near-surface compressional and shear wave speeds constrained by body-wave polarization analysis. *Geophysical Journal International*, *213*(3), 1559–1571. https://doi.org/10.1093/gji/ggy072

Price, A. N., Lindsey, C., Fairley, J. P., & Larson, P. B. (2015). Imaging near-surface controls on hot spring expression using shallow seismic refraction in Yellowstone National Park. *AGU Fall Meeting Abstracts*. V12B-01.

Reed, M. H., Munoz-Saez, C., Hajimirza, S., Wu, S.-M., Barth, A., Girona, T., et al. (2021). The 2018 reawakening and eruption dynamics of Steamboat Geyser, the world's tallest active geyser. *Proceedings of the National Academy of Sciences*, *118*(2), e2020943118.

Richards, P. G., Waldhauser, F., Schaff, D., & Kim, W. Y. (2006). The applicability of modern methods of earthquake location. *Pure and Applied Geophysics*, *163*(2–3), 351–372.

Rinehart, J. S. (1965). Earth tremors generated by Old Faithful geyser. *Science*, *150*(3695), 494–496.

Rudolph, M. L., & Sohn, R. A. (2017). A model for internal oscillations in geysers, with application to Old Faithful (Yellowstone, USA). *Journal of Volcanology and Geothermal Research*, *343*, 17–24.

Rudolph, M. L., Sohn, R. A., & Lev, E. (2018). Fluid oscillations in a laboratory geyser with a bubble trap. *Journal of Volcanology and Geothermal Research*, *368*, 100–110.

Shapiro, N. M., Campillo, M., Stehly, L., & Ritzwoller, M. H. (2005). High-resolution surface-wave tomography from ambient seismic noise. *Science*, *307*(5715), 1615–1618.

Vandemeulebrouck, J., Roux, P., & Cros, E. (2013). The plumbing of Old Faithful Geyser revealed by hydrothermal tremor. *Geophysical Research Letters*, *40*, 1989–1993. https://doi.org/10.1002/grl.50422

Vandemeulebrouck, J., Sohn, R. A., Rudolph, M. L., Hurwitz, S., Manga, M., Johnston, M. J. S., et al. (2014). Eruptions at Lone Star geyser, Yellowstone National Park, USA: 2. Constraints on subsurface dynamics. *Journal of Geophysical Research: Solid Earth*, *119*, 8688–8707. https://doi.org/10.1002/2014JB011526

Walter, T. R., Jousset, P., Allahbakhshi, M., Witt, T., Gudmundsson, M. T., & Hersir, G. P. (2018). Underwater and drone based photogrammetry reveals structural control at Geysir geothermal field in Iceland. *Journal of Volcanology and Geothermal Research*, *391*, 106282. https://doi.org/10.1016/j.jvolgeores.2018.01.010

White, D. E., Fournier, R. O., Muffler, L. J. P., & Truesdell, A. H. (1975). Physical results of research drilling in thermal areas of Yellowstone National Park, Wyoming, U.S. Geological Survey Professional Paper 892 (70 p.).

White, D. E., Hutchinson, R. A., & Keith, T. E. C. (1988). The geology and remarkable thermal activity of Norris Geyser Basin, Yellowstone National Park, Wyoming, USGS Professional Paper 1456.

Wicks, C. W., Dzurisin, D., Lowenstern, J. B., & Svarc, J. (2020). Magma intrusion and volatile ascent beneath Norris Geyser Basin, Yellowstone National Park. *Journal of Geophysical Research: Solid Earth*, *125*, e2019JB018208. https://doi.org/10.1029/2019JB018208

Wu, S.-M., Lin, F.-C., Farrell, J., & Allam, A. (2019). Imaging the deep subsurface plumbing of Old Faithful geyser from low-frequency hydrothermal tremor migration. *Geophysical Research Letters*, *46*, 7315–7322. https://doi.org/10.1029/2018GL081771

Wu, S.-M., Ward, K. M., Farrell, J., Lin, F.-C., Karplus, M., & Smith, R. B. (2017). Anatomy of Old Faithful from subsurface seismic imaging of the Yellowstone Upper Geyser Basin. *Geophysical Research Letters*, *44*, 10240–10247. https://doi.org/10.1002/2017GL075255